Cryo-electron tomography reveals postsynaptic nanoblocks in excitatory synapses for transcellular alignment

Rong Sun[1], Liana Wilson[1], Mariam Haider[1,2], Baris Alten[3,6], Zimeng Zhou[1,4], Xinyi Wang[1,5], Qiangjun Zhou[1*].

[1] Department of Cell and Developmental Biology, Vanderbilt Brain Institute, Center for Structural Biology, Vanderbilt Kennedy Center, Vanderbilt University, Nashville, TN, 37240, USA.

[2] Center for Structural Biology Cryo-EM Facility, Vanderbilt University, Nashville, TN, 37240, USA.

[3] Department of Pharmacology, Vanderbilt University, Nashville, TN, 37212, USA.

[4] School of Engineering, Vanderbilt University, Nashville, TN, 37212, USA.

[5] Peabody College, Vanderbilt University, Nashville, TN, 37212, USA

[6] Present address: Harvard Medical School, Boston, MA, 02115, USA and Department of Neurology, Massachusetts General Hospital and Brigham & Women's Hospital, Boston, MA, 02115, USA

Abstract

The nanoscale organization of proteins within synapses is critical for maintaining and regulating synaptic transmission and plasticity. Here, we use cryogenic electron tomography to directly visualize the *in situ* three-dimensional architecture and supramolecular organization of transsynaptic alignment of pre-cleft-postsynaptic components in their native cellular context in both synaptosomes from rat hippocampi and synapses from rat primary cultured neurons. High-resolution electron microscopy and quantitative analyses reveal that release sites align with adhesion molecules, receptor clusters, and postsynaptic density (PSD) nanoblocks as a physical, transsynaptic, nano-alignment. Additionally, it has been determined that the PSDs contain different-sized, membrane-associated, subsynaptic protein nanoblocks. Furthermore, large nanoblocks are formed by small nanoblocks positioned close enough together. Lastly, the tomograms of synaptosomes allow us to detect the glutamate receptor-like particles by subtomogram averaging at resolutions of 24 Å and 26 Å. The results of this study provide a more comprehensive understanding of synaptic ultrastructure and demonstrate that PSD is organized into subsynaptic nanoblocks to form transcellular alignment.

Introduction

Cellular function is driven by nanoscale spatial organization of multi-protein assemblies and their interactions with other molecular components and cellular organelles. Typical examples of such nanoscale structures are neuronal chemical synapses. These are the most complex cell-cell junctions, with more than 2,000 distinct synaptic proteins.[1] In particular, laboratories have been accumulating evidence that multiple presynaptic, postsynaptic, and cell-adhesion proteins in excitatory synapses are finely organized in lipid-bound nanoscale structures to facilitate extremely rapid, dynamic, efficient, and tightly regulated transmission of information between neurons[2-10]. Moreover, the activity-dependent rearrangement of these synaptic proteins, including neurotransmitter receptors and other synaptic proteins, plays a key mechanistic role in synaptic plasticity. Synaptic plasticity is essential for perception, decision making, learning, and memory formation.

Recent studies provide evidence for the high-level organization of nanoscale supramolecular assemblies spanning the synaptic cleft, giving rise to *nanocolumns* of juxtaposed pre- and postsynaptic compartments in excitatory synapses[3,4,11-16]. Specifically, presynaptic active-zone scaffold proteins, such as RIM, form nanodomains that define synaptic vesicle docking and release sites. These sites align with clustered neurotransmitter receptors such as α-amino-3-hydroxy-5-methyl-4-isoxazolepropionic acid receptor (also known as AMPAR) and postsynaptic scaffolding proteins such as PSD95 via adhesion proteins in the synaptic cleft[10,17,18].

The postsynaptic density (PSD) appears in conventional electron micrographs as an electron-dense lamina just beneath the postsynaptic membran.[19]. A PSD meshwork model comprising regularly spaced vertical filaments was proposed based on electron microscopy (EM) and biochemical assays[20-24]. Two additional forms of PSD organization have been proposed: nano-domains based on super-resolution imaging[3-5,25,26], and liquid condensate based on *in vitro* PSD mixing assay[27-29]. All these studies provide more evidence for the high-level organization of nanoscale supramolecular assemblies in the synapse, indicating that synaptic proteins are not randomly distributed and instead form functional synaptic nanostructures. However, nanoscale organization of the PSD and postsynaptic receptors is largely unknown due to the technical challenges imposed by synaptic molecular complexity.

Cryo-electron tomography (cryo-ET) is a powerful technique that produces three-dimensional (3D) volume reconstructions, or *tomograms*, of macromolecular and subcellular biological structures in their native context at nanometer resolution. To prevent producing artifacts through chemical fixation, dehydration, and heavy-metal staining, biological samples are rapidly frozen to obtain a "true, instantaneous snapshot"[30-33]. In general, obtaining high-quality data requires cryo-ET samples to be thin enough for electrons to pass through (~200 nm), posing a technical challenge during sample preparation, which limits the resolution of cellular cryo-ET[34]. The resolution is also limited by the crowded cellular environment. To overcome these limitations, isolated synaptic terminals have been used for cryo-ET studies to decrease sample thickness[10,35]. A classic type of isolated synaptic terminal called a *synaptosome* is highly suitable for cryo-ET, because it retains a piece of attached postsynaptic membrane that faces the

active zone[36,37]. Synaptosomes help to improve the resolution, as the average thickness of a synaptosome is 200-300 nm with the core of PSD in our preparations. Here, we developed a simplified sample preparation workflow to obtain the synaptosomes from mature rat hippocampi, achieving high-resolution synaptic nanostructures with cryo-ET and sub-tomogram averaging. With this method, we directly visualized the overall architecture of the transcellular alignment in excitatory synapses. Our results revealed that PSD is formed by subsynaptic PSD nanoblocks of specific sizes. We also determined *in situ* structures of two types of putative ionotropic glutamate receptor-like particles at 24-Å and 26-Å resolution. Finally, we demonstrated subsynaptic organization of PSD nanoblocks, as well as the physical transcellular alignment between tethered synaptic vesicles and PSD nanoblocks in intact synapses within rat primary cultured hippocampal neurons.

Results

Physical transsynaptic alignment in synaptosomes

To study subsynaptic organization, we prepared synaptosomes via a simplified workflow. After dissecting the hippocampi from rat brains, we performed four strokes of homogenization and a 10-minute centrifugation at 800 *g,* followed by plunge-freezing and cryo-ET data acquisition (Supplementary Fig. 1a). Our preparations included two different types of isolated synaptic terminals based on their morphology: Synaptosomes retained a patch of postsynaptic membrane with PSD (Fig. 1 and Supplementary Fig. 1b-e, see also Supplementary Video 2), while synaptoneurosomes retained an enclosed postsynaptic compartment (Supplementary Fig. 1f-i)[38,39]. For this study, we primarily focused on synaptosomes as we were able to achieve higher-resolution structural information from these relatively thin and molecularly- uncrowded samples compared to synaptoneurosomes and intact synapses. We acquired 60 high quality tomograms of isolated synaptic terminals (40 synaptosomes and 20 synaptoneurosomes), which enabled us to directly visualize characteristic features of a neuronal synapse, including typical synaptic proteins (Fig. 1a, 1b and Supplementary Fig. 1p-u). In all our preparations, we were able to find synaptosomes and synaptoneurosomes and did not observe obvious morphological differences in synaptosomes or synaptoneurosomes at nanoscale between batches of sample preparations. To ensure the data consistency in PSD density analyses and subtomogram averaging, all 60 tomograms used were from the same data collection session and from the same batch of sample preparation. All the synaptosomes we obtained were likely from excitatory synapses, as they have thick PSDs of more than 30 nm, which is a known feature of excitatory synapses[19,22].

To study the relationship between release sites, adhesion molecules, postsynaptic densities, and synaptic receptors, we scrutinized the tethered synaptic vesicles that indicate the position of synaptic release sites. We also investigated the corresponding nanostructures in the cleft and in the postsynaptic compartment. Examining the electron densities and measuring the gray values of synaptosome tomograms (Fig. 1c and Supplementary Fig. 1p-s) allowed us to detect the adhesion molecule-like proteins and membrane proteins in the synaptic cleft, as well as the PSD protein clusters, or which we call *nanoblocks*. The tomographic slice in Fig. 1c's left panel shows protein densities in

the middle of the cleft, which we posit to be the adhesion molecules, as well as a density layer on the postsynaptic membrane that is comprised of membrane proteins. These direct visualizations are consistent with the density plot in Fig. 1c's right panel. Some of the postsynaptic membrane proteins are most likely synaptic receptors, based on their geometry and size (see Methods regarding the criteria to select particles for subtomogram averaging). We found that synaptosomes and synaptoneurosomes have specific cleft widths (Fig. 1d); and the clefts of synaptosomes tend to be wider than those of synaptoneurosomes (39.7 ± 0.9 nm for synaptosomes n = 33; and 30.5 ± 0.9 nm for synaptoneurosomes n = 20). Of note, 7 synaptosomes were not included in these measurements as the postsynaptic membranes were not parallel to the presynaptic membranes. This might be due to different adhesion molecules surviving the sample isolation process, thus resulting in different widths of synaptic clefts. We observed that tethered vesicles aligned with the adhesion-like molecules, the membrane protein-like particles, and PSD densities (Fig. 1e-i). This direct visualization of pre-cleft-postsynaptic alignment suggests that postsynaptic receptors, which anchored by PSD scaffold proteins, are aligned with presynaptic release sites through adhesion molecules in the synaptic cleft. Two examples of adhesion-receptor-PSD nanoblock alignment without a tethered synaptic vesicle are also shown here, indicating these might be potential release sites (Fig. 1j-k).

PSD subsynaptic organization in synaptosomes

Next, we investigated PSD densities and performed quantitative analyses on the PSD nanoblock dimensions. A representative tomogram of a synaptosome acquired by cryo-ET is shown in Fig. 2a, in which PSD nanoblocks (indicated by red arrows) are clearly visualized beneath the membrane. In terms of the overall PSD electron density patterns, this result is consistent with previous EM studies stating that the core of the PSD is dominated by vertically oriented filaments[20,40] or spiky structures[24]. In our results, there were roughly three types of synaptosomes based on the organization of the PSD: synaptosomes with separated PSD nanoblocks; synaptosomes with both separated and continuous PSD nanoblocks; and synaptosomes with continuous PSD (Supplementary Fig. 1j-o). To delineate the PSD nanostructures of all three synaptosome types, we applied the following quantitative analysis: First, we measured gray values of protein densities of a 40-nm thick PSD area beneath the postsynaptic membrane (Fig. 2a-b). Then, we combined 2D gray values across a series of continuous virtual tomographic slices, generating a gray value density map (Fig. 2c, top panel). With normalization and filtering processing, **d**ensity-**b**ased **s**patial **c**lustering of **a**pplications with **n**oise (DBSCAN) results show projected PSD density nanoblocks in the 40-nm range from the postsynaptic membrane (Fig.2c, bottom panel). DBSCAN is a density-based clustering non-parametric algorithm[41] and it is widely used in biological data analysis[42,43]. We next measured the area and width of each protein nanoblock (Fig. 2c-d). The area of nanoblock was defined as its convex hull area shown by encircling red lines. The width of nanoblock was defined as the largest x-axis distance between two pixels in each cluster. Fig. 2d shows examples of nanoblocks with different areas and widths quantified by the DBSCAN clustering method. Multiple peaks were detected in the area distribution

of nanoblocks from all synaptosomes (Fig. 2e), while the width distribution was fit with two peaks (Fig. 2f). Distinct fitting peaks in the area distribution histogram indicate that nanoblocks have distinct sizes, and that large nanoblocks may be composed of several small nanoblocks, which is also supported by examining the morphology of some nanoblocks with large widths (Fig. 2d). Though the geometric shape of the nanoblock was irregular, the way we quantified the width reflected the dimension of the nanoblock in x axis, while the dimension of nanoblock in z axis was affected by the missing wedge effect. Overall, our analysis suggests that PSD nanoblocks can be positioned closely enough to one another to form large nanoblocks and coordinate synaptic function.

To further analyze the size and morphology of subsynaptic nanoblocks, we measured the heights of the protein nanoblocks obtained via DBSCAN clustering. The height was quantified based on gray values along the nanoblock at its largest length (Fig. 1c). The distribution of nanoblock heights reveals that most nanoblocks are in the 30~60 nm range, while a small population is below 20 nm or above 80 nm (Fig. 2g). The large nanoblocks shown on the right side of Fig. 2h appear to be composed of multiple small protein nanoblocks, which were positioned close together in our clustering analysis. The two schematics on the right side of Figure 2H show these large nanoblocks' morphology. Their heights are also variable. Additionally, we analyzed the gap between PSD nanoblocks. The distance between each nanoblock centroid (Fig. 2i) and the nearest distance between each nanoblock edge (Fig. 2j) together describe the spacing between nanoblocks, suggesting that the gaps with less protein densities segmented the PSD. Overall, our analysis demonstrates that subsynaptic nanoblocks of different sizes form the PSD.

In situ **organization of receptor-like particles on the postsynaptic membrane**

To further investigate the molecular organization of nano-alignment, we employed the subtomogram averaging method to detect glutamate receptors in our synaptosome samples. AMPARs or n-methyl-d-aspartate receptors (NMDARs) are prominent receptors in excitatory synapses and consist of N-terminal domains (NTD) and ligand binding domains (LBD) within the synaptic cleft[44-46]. We manually selected 1,565 particles from 28 synaptosomes with NTD and LBD in the range from 10 nm to 14 nm for subtomogram averaging (Fig. 3a and Supplementary Fig. 3a). Eventually, we achieved an averaged structure of type A receptor with 391 particles (Fig. 3b-e) and an averaged structure of type B receptor with 189 particles (Fig. 3f-i). The type A receptor is structurally similar to the O-shape AMPAR (PDB: 5ide), while the type B receptor is structurally similar to the Y-shape AMPAR (PDB: 6qkz). In previous studies, the extracellular N-termini of Y-shape AMPARs were determined to be ~14 nm in height[47,48], while the extracellular N-termini of O-shape AMPARs were found to be ~10 nm[49], and the extracellular N-termini of NMDARs were ~11 nm in height[50,51]. Considering the morphology similarity of N-termini between O-shape AMPAR and NMDAR at the resolution we achieved (Supplementary Fig. 3b), it is difficult to exclude the possibility that some NMDARs were also counted in the type A receptor population.

To study the distribution of the averaged receptors, we anchored the type A and type B receptors to the PSD clustering results. As displayed in Fig. 3j, three examples demonstrate that some of the averaged receptors (type A receptors and type B receptors) are within PSD nanoblocks, while there are also receptors outside of the PSD clusters. We also identified some particles that remained unclassified and were neither type A nor type B receptors. Among these undefined particles, some are within, and some are outside of the PSD nanoblocks. Previous studies show that AMPAR and NMDAR are targeted on the postsynaptic membrane by scaffolding proteins within the PSD[52-56]. However, the protein nanoblocks represent the core of the PSD; and it is possible that these particles which do not fall onto the PSD nanoblocks, are responsible for scaffolding by interacting with proteins outside of the nanoblocks. Compared to the type B receptors, the nearest neighbor distance analysis indicates that the type A receptors are more clustered (Fig. 3k-l). The number of type A and type B receptors varies in all synaptosomes (Fig. 3m), showing the heterogeneity of the synaptosomes.

PSD subsynaptic organization in intact neurons

We also examined the subsynaptic organization of synapses to determine whether similar subsynaptic nanoblocks identified in synaptosomes can also be found in intact synapses from cultured neurons. To accomplish this, we seeded dissociated primary hippocampal neurons on gold EM grids and examined the synaptic ultrastructure in intact neurons using cryo-ET (Supplementary Fig. 4a-e). In reconstructed tomograms, a typical synapse consists of a presynaptic compartment with a population of synaptic vesicles, a synaptic cleft, and a postsynaptic compartment with PSD. We also focused on excitatory synapses and excluded synapses with thin PSDs in cultured neurons from our analysis (Supplementary Fig. 4f-h).

We collected 211 tilt series of synapse-like structures from the wild-type primary hippocampal neurons and reconstructed them. 131 of the reconstructed tomograms were synapses, and 121 synapses had thick PSDs. Three examples of excitatory synapses are shown in Fig. 4. Tomographic slices (Fig. 4a, x, f, h, k, and m) and segmented structures (Fig. 4b and g, see also Supplementary Video 2) display PSDs' protein densities, suggesting that protein distribution is not homogeneous within the PSD. However, the crowded molecular environment and overall thickness of neurons rendered a low signal-to-noise ratio in the cellular context, making patterns of protein complexes difficult to recognize and analyze. Using the software package IsoNet[57], we performed contrast transfer function (CTF) deconvolution and corrected the missing wedge effect to enhance contrast in 32 out of 121 cryo-electron tomograms of excitatory synapses. Following IsoNet correction, tomographic slices show more obvious protein nanoblocks in the PSDs (Fig. 4d, i, and n). Quantitative characterization of the PSDs' 3D volume (Fig. 4e, j, and o) indicates that proteins distribute unevenly within the PSD and form subsynaptic nanoblocks. The nanoblocks' area and distance (Fig. 4p-r) show similar distributions to those from our synaptosome datasets. Our observations suggest that in intact synapses, there are nanoblocks of different sizes consisting of postsynaptic proteins, similar to those were observed in synaptosomes. Additionally, multiple tethered vesicles, docked

vesicles, or fused vesicles represent release sites (Supplementary Fig. 4i-n) and tend to align with large PSD nanoblocks (Fig. 4i and o).

Discussion

In this study, we utilized cryo-ET to directly visualize the ultrastructure of excitatory synapses in their near-native state within purified hippocampal synaptosomes from 10-week-old young adult rats as well as primary hippocampal neurons cultured from postnatal day 0 newborn rats. Importantly, we found that in our synaptosome samples, the exposed postsynaptic membranes remain attached to the presynaptic terminals. The only components remaining were the membrane-associated PSD core components (PSD nanoblocks), while weakly interacting proteins (in PSD gaps) and other postsynaptic components might be lost. This allowed us to study the core PSD components against a relatively clean background. Meanwhile, studies of the whole synapse in intact cultured neurons provided more physiological and complete ultrastructure features. With these two different samples, we consistently recorded the physical transsynaptic alignment and subsynaptic organization in the form of PSD nanoblocks. Our observations suggest that membrane-associated PSD core components within synaptosomes are relatively stable, and that they maintain structural integrity during the isolation process for synaptosome preparation via our simplified protocol. This finding is consistent with previous observations that PSD complexes and the PSD membranes are detergent-resistant and stable enough to be purified from conventional synaptic fractions[58-60]. Thus, it is likely that the nanoscale organization and basic ultrastructure features we observed also reflect synaptic architecture within the brain.

An alignment between pre- and postsynaptic elements has long been proposed but was only recently reported and named a *nanocolumn*, discovered through super-resolution light microscopy[3]. Thus far, only labeled synaptic proteins such as PSD95, receptors, and RIM have been shown to form nanoclusters as a part of nanocolumns. Our cryo-ET approach allows us to examine the molecular organization of all cellular components at molecular resolution, as well as the physical alignment of subsynaptic nanostructures[30-32,61]. As such, this study provides direct evidence supporting the nanocolumn hypothesis with higher-resolution structural information, particularly through direct visualization of potential release sites indicated by tethered, docked, and fused vesicles aligning with PSD nanoblocks both in synaptosomes and intact synapses from hippocampal cultures. We also observed that multiple release sites aligning with a large PSD nanoblock is common (Fig. 4). Though, it should be noted that fewer tethered, docked, or fused vesicles were found in synaptosomes due to our isolation process. While most of these tethered vesicles aligned with PSD nanoblocks and adhesion-like proteins, as well as a cluster of receptors (Fig. 1e-i), there may be more undetected release sites (Fig. 1j-k). Further improvements in cellular tomography will surely enable direct visualization of individual synaptic proteins in cultured neurons or brain tissues. These discoveries will provide us with ultrastructure information at a more natural state.

The PSD in the excitatory postsynaptic terminal is a dense area packed with postsynaptic

proteins, where hundreds of molecules have been identified[62,63]. Efforts have been made to clarify the PSD's molecular organization and the synaptic functions that these PSD proteins serve. The development of imaging techniques such as super-resolution fluorescent microscopy has facilitated the discovery of subsynaptic protein clusters, or *nanodomains*[3-5,64]. These nanodomains are ~70 to 160 nm in size, which is larger than most protein nanoblocks we visualized within the PSDs of synaptosomes. Therefore, we postulate that the small nanoblocks we discovered within the PSD may be a structural unit that forms the nanodomain, which in turn forms the PSD. A nanoblock consists of certain copies of several different scaffold proteins that form a supramolecular structure, which links to certain copies of synaptic receptors and aligns with the presynaptic release sites through adhesion molecules. However, in considering the diversity of PSD protein complexes[65-68], it remains possible that the composition of different-sized PSD nanoblocks varies.

Chemical fixation, or high-pressure freezing and freeze substitution EM sample preparation, displays a PSD mesh model[20,24,69]. Using cryo-ET, we also observed vertical filaments within synaptosomes and intact synapses, which were smaller in size. We suspect that the size difference is due to the inherent differences between sample preparation methods and imaging modalities. In the liquid condensate mode of PSD[27-29], the liquid droplet is at micron scale. It is possible that the synaptic proteins in cells form nanoblocks or nanoclusters following the same mechanism as in the *in vitro* PSD protein mixing assay.

Subtomogram averaging of receptor-like particles produced a 24-Å and a 26-Å structure from a small number of particles (Supplementary Fig.3). We believe that we failed to achieve higher resolutions due to AMPARs having different reconfigurations secondary to interactions between AMPARs' flexible extracellular domains and other proteins[44,47,70-73]. The ligand proteins and neighboring proteins also contribute to the density, rendering each receptor structurally heterogenous. Overcoming these difficulties in observing high-resolution structures of synaptic receptors, as well as linking AMPARs' *in situ* conformation information with their functional states, would require an enormous cryo-ET dataset of synaptosomes or synapses with proper thickness.

Here we propose a nanoscale organization model at excitatory synapses (Fig. 4s). The model is supported by our data from synaptosomes and cultured neurons (Fig. 1-4), showing the commonality and diversity across synapses. Different-sized PSD nanoblocks and their organizing model within the transcellular alignment at the synapse suggest a potential mechanism for PSD nanoblocks to regulate synaptic strength. Evidence from super-resolution and EM studies also suggests that synaptic activity affects the number and size of PSD nanoclusters or densities[4,74-76]. In addition, this model may explain two seemingly contradictory properties of the PSD: stable, yet dynamic. PSD proteins form stable, similarly sized nanoblocks, enabling them to recruit other postsynaptic proteins to form dispersed nanoblocks or clustered nanoblocks (Fig. 4s) in response to neuronal activity[77].

Figure Legends

Fig. 1. A presynaptic release site correlates with adhesion molecules, membrane proteins, and PSD nanoblocks.

(a) A tomographic slice showing an excitatory synaptosome. (b) 3D segmentation of the synaptosome shown in panel A. (c) Quantification of the synaptic cleft and the PSD shown in panel A. The zoomed-in tomographic slice showing the excitatory synaptosome from panel A is on the left and its density plot showing gray values along the red solid line is on the right. (d) Cleft widths of synaptosomes and synaptoneurosomes. (e-k) Examples of transsynaptic alignment of adhesion molecules and postsynaptic membrane proteins in the cleft, as well as PSD nanoblocks in the postsynapse. Tethered synaptic vesicles also align with cleft and PSD densities. Scale bars: (a-b) 100 nm; (e-g) 20 nm. *Abbreviations PreSM: Presynaptic membrane. PostSM: Postsynaptic membrane. PostMP: Postsynaptic membrane protein.*

Fig. 2. PSD subsynaptic organization in synaptosomes.

(a) Top panel: A tomographic slice showing the subsynaptic nanoblocks of a synaptosome. Arrows and numbers indicate the seven protein clusters in the PSD. Bottom panel: 3D segmentation of the synaptosome in the top panel. (b) Density plot shows average gray values along the 40-nm blue bar in the top panel of (a). (c) 3D density analysis in the PSD of synaptosome in (a). Top panel: Density plot shows gray values of 40-nm PSD density projected to the xz plane. The blue dotted line indicates the plane of the tomographic slice shown in (a). Bottom panel: DBSCAN clustering result of 40-nm PSD density projected to the xz plane. (d) Examples of PSD nanoblocks in 2D tomographic slices and corresponding projected DBSCAN clustering results. Values in each panel indicate the width (Units: nm) of the PSD block. The blue dotted lines indicate the plane of the corresponding tomographic slices. (e) Distribution of PSD nanoblock area. (f) Distribution of PSD nanoblock width. (g) Distribution of nanoblock height. (h) Scatter plot of PSD nanoblock area to its height. Vertical lines are the peak values of gaussian fitting in (e). Schematics in four corners show corresponding nanoblock morphology in the scatter plot. (i) Distribution of nearest neighbor distance between PSD nanoblock centroids. (j) Distribution of distance between nearest pixels of PSD nanoblocks. Scale bars: (a, c) 50 nm; (d) 20 nm.

Fig. 3. Subtomogram averaging of receptor-like particles on the postsynaptic membrane.

(a) Receptor-like particles on the postsynaptic membrane. (b-i) Subtomogram averaged type A receptor and type B receptor. Models from PDB bank are fitted to the averaged electron densities. Yellow: PDB 5ide. Red: PDB 6qkz. (j) Examples of type A receptors, type B receptors, and undefined particles on the postsynaptic clusters. (k-l) Nearest neighbor distances of type A receptor (k) and type B receptor (l). (m) Type A and type B receptor numbers in each synaptosome. Scale bars: (a) top panel 100 nm, bottom panel 20 nm; (b-i) 5 nm; (j) 50 nm.

Fig. 4. PSD subsynaptic organization in intact neurons.

(a) Tomographic slice of an excitatory synapse. (b) Segmentation of the synapse in (a). (c) Zoom-in view of the synapse in (a). (d) IsoNet-corrected tomographic slice of (c). Red arrowheads indicate PSD nanoblocks. (e) Clustering results of 40-nm PSD density projected to the plane parallel to the postsynaptic membrane. Each color represents one cluster. Docked or tethered vesicle positions are marked as circles. (f) Tomographic slice of a second excitatory synapse. (g) Segmentation of the synapse in (f). (h) Zoom-in view of the synapse in (f). (i) IsoNet-corrected tomographic slice of (h). Red arrowheads indicate PSD nanoblocks. (j) Clustering results of 40-nm PSD density projected to the plane parallel to the postsynaptic membrane. Each color represents one cluster. Docked or tethered vesicle positions are marked as circles. (k) Tomographic slice of a third excitatory synapse. (l) Segmentation of the synapse in (k). (m) Zoom-in view of the synapse in (k). (n) IsoNet-corrected tomographic slice of (m). Red arrowheads indicate PSD nanoblocks. (o) Clustering results of 40-nm PSD density projected to the plane parallel to the postsynaptic membrane. Each color represents one cluster. Docked or tethered vesicle positions are marked as circles. (p) Distribution of PSD nanoblock area. (q) Distribution of nearest neighbor distance between PSD nanoblock centroids. (r) Distribution of distance between nearest pixels of PSD nanoblocks. (s) Working model of subsynaptic organizations. Parameter ranges of nanoblock edge distance, centroid distance and nanoblock width are FWHM (the full width at half maximum) of single-peak gaussian fitting. Scale bars: (a, b, f, g, k, l) 100 nm; (c-e, h-j, m-o) 50 nm.

Acknowledgments

We thank Drs. Ege T. Kavalali, Terunaga Nakagawa, William Wan, Roger J Colbran and Mark E. Bowen for stimulating discussions and critical reading of the manuscript; the NIH for support (R00 MH113764 to Q.Z.); the Vanderbilt Faculty Fellowship Endowment Fund; and “Neurodegenerative” TIPS Initiative Award for support.

EM data collections were conducted at the Center for Structural Biology Cryo-EM Facility at Vanderbilt University. We also acknowledge the use of the Glacios cryo-TEM, which was acquired by NIH grant 1 S10 OD030292-01.

Author contributions

Conceptualization, R.S. and Q.Z.; Methodology, R.S. and Q.Z.; Investigation, R.S. and Q.Z.; Experiments, R.S. and B.A., Data analysis, R.S., L.W., M.H., X.W. and ZM.Z.; Writing – Original Draft, R.S. and Q.Z.; Writing – Review & Editing, R.S., L.W., M.H., X.W., ZM.Z. and Q.Z..; Funding Acquisition, Q.Z..

Competing interests

The authors declare no competing interests.

413 **Methods**

414 **Synaptosome isolation**

415 10-week Sprague-Dawley rats with either sex were used for synaptosome isolation. The
416 rats were kept in 12 hours: 12 hours dark:light cycle and provided with treats as well as
417 cardboard enrichments before the experiments. The rats were deeply anesthetized with
418 isoflurane. Hippocampi tissue were dissected in the ice-cold homogenization buffer
419 containing 0.32 M sucrose, 4 mM Hepes, 1mM EDTA, at pH 7.4 Then the tissue was
420 homogenized at ~500 rpm for 4 strokes using an overhead stirrer (Electron Microscopy
421 Sciences 6480610) and a tissue grinder (Electron Microscopy Sciences 6479310) in the
422 ice-cold homogenization buffer. After homogenization, the homogenates were
423 centrifuged at 800g at 4 °C for 10 min. The supernatant was immediately taken for cryo-
424 ET sample preparation. All animal procedures were performed in accordance with the
425 guide for the care and use of laboratory animals and were approved by the Institutional
426 Animal Care and Use Committee at Vanderbilt University.

427 **Primary dissociated neuronal cultures**

428 The protocol was modified from previous works[22,78,79]. Postnatal day 0 Sprague-Dawley
429 rats of either sex were used for primary hippocampal cultures. Pregnant Sprague-Dawley
430 rats were housed individually until they give birth to a litter and were kept in 12 hours: 12
431 hours dark:light cycle. The pregnant rats were provided with the same treats as well as
432 cardboard enrichments. Postnatal day 0 littermates were used to prepare primary
433 dissociated neuronal cultures. Hippocampi were dissected in ice cold 20% fetal bovine
434 serum (FBS) containing Hanks' balanced salt solution. Tissues were then washed and
435 treated with 10 mg/ml trypsin and 0.5 mg/ml DNase at 37 °C for 10 min. The tissues
436 were washed again, dissociated using filtered P1000 tip and centrifuged at 1000 rpm for
437 10 mins at 4 °C. Pellet containing neurons was resuspended in Neurobasal Plus medium
438 supplemented with GlutaMAX-I and B27 supplement. Neurons were plated onto
439 Quantifoil R2/2 Au 200 EM grids coated with poly-L-lysine. Cultures were kept in
440 humidified incubators at 37 °C and gassed with 95% air and 5% CO2. On DIV1, the
441 neurobasal plus medium was replaced with 4 µM cytosine arabinoside containing
442 neurobasal plus medium. On DIV4, the cytosine arabinoside concentration was dropped 2
443 µM by performing a half media change. Cultures were kept without any disruption until
444 DIV14. The cultures on EM grids were plunged frozen between DIV14-18, when
445 synapses reached maturity. All animal procedures were performed in accordance with the
446 guide for the care and use of laboratory animals and were approved by the Institutional
447 Animal Care and Use Committee at Vanderbilt University.

448

449 **Synaptosome and neuronal culture vitrification**

450 Synaptosome

451 FEI Vitrobot Mark III was used for the plunge freezing. Set the parameters of the plunge
452 freezer as follows: humidity 100%, temperature 4 °C, blot time 3.5 s, blot total 1, blot

offset -1.5, and wait time 6 s. Supernatant after centrifugation mixed with 10-nm gold beads solution (Aurion, cat # 25486) at 1:1 ratio was added to the mounted grid (Quantifoil R2/2 Cu 200 EM). The grids were plunged into liquid nitrogen cooled liquid ethane for rapid vitrification and were stored in liquid nitrogen until use.

Primary dissociated neuronal cultures

The vitrification process of neuronal cultures is similar to the synaptosome with a few modifications. The culture dishes were taken out from the incubator on DIV 14-18. The culture medium was replaced with a modified Tyrode's solution containing the followings was used: (in mM): 150 NaCl, 4 KCl, 1.25 $MgCl_2$, 2 $CaCl_2$, 10 D-glucose, 10 Hepes at pH 7.4. After setting up the plunge freezer as follows: humidity 100%, temperature 22 °C, blot time 3.5 s, blot total 1, blot offset -1.5, and wait time 6 s, the grids with cultures were mounted. 4 µL 10-nm gold beads solution was added to the mounted grid before plunging. After rapid vitrification, the grids were stored in liquid nitrogen until use.

Cryo-ET data collection

Automated batch tilt series collection was done with Thermo Fisher Tomography5 software on Thermo Fisher Titan Krios G4 using the Gatan K3 camera in zero-loss mode (slit width 20 eV). The tilt series of neuronal cultures were collected using the dose-symmetric scheme[80] starting from 0° to ± 60° with an interval of 2°, and with the defocus value at -7 µm, with the total electron dosage of ~150 $e^-/Å^2$ which were evenly distributed between tilts. The final pixel size was 3.3 Å with 26000× magnification. The tilt series of synaptosomes were collected with Voltage Phase Plate. The phase plate dataset was collected at the pixel size 3.3 Å with 26000× magnification, using the dose-symmetric scheme starting from 0° to ± 60°with an interval of 2°, and with the defocus value at -2 µm. The total electron dosage of ~150 $e^-/Å^2$ was evenly distributed between tilts. The phase plate was switched to a new position and activated to gain a phase shift of around 0.3π prior to each tilt series. Conditioning of the phase plate was also performed between each tilt.

Data reconstruction and subtomogram averaging

Tomograms of synaptosome at pixel size of 3.3 Å with phase plate were used for subtomogram averaging. Synaptosome thicker than 500 nm were excluded, and 28 tomograms were selected. TOMOMAN package[81] was used to preprocess the data. The workflow of TOMOMAN included motion correction by MotionCorr2[82], image sorting, dose filtering and CTF estimation by Gctf [83]. Then the tilt series were aligned the reconstructed using IMOD[84]. Fine alignment of the tilt series was performed by using the 10 nm gold beads (Aurion, cat # 25486) as fiducial markers. Both back projection and

back projection with five-iteration SIRT (simultaneous iterative reconstruction technique)-like were performed to reconstruct each tilt series. Segmentation and 3D rendering were done using IMOD. In the synaptosome dataset, 1565 receptor-like particles were picked according to the size and shape. Only the particles around 10 ~14 nm on the postsynaptic membrane with LBD (ligand binding domain) and ATD (Amino terminal domain) were included. Subtomogram averaging was done using RELION 3.0.8[85]. We applied a box size of 96 using unbinned data. First, we generated the initial model using 3d auto-refine with the unbinned data without applying symmetry. 3d classification resulted in two good classes. After 3d classification, we generated 3d initial models for each class respectively with C2 symmetry and did 3d auto-refine for each class using the corresponding initial models. Manual repicking of the particles was performed to exclude the particles which were too close (distance < 8 nm) and final averaging was performed using the remaining particles in 3d auto-refine.

PSD density analysis and quantification

Density of PSD was measured using following method. In the synaptosome dataset, synaptosome with a PSD close to cryo grid carbon hole were excluded as the gray values were affected by the hole edge. Synaptosomes thicker than 500 nm and synaptosomes with the postsynaptic membrane not parallel to its presynaptic membrane were also excluded. 16 tomograms were selected for PSD density clustering analysis. In the culture neuron dataset, synapses thicker than 700 nm were excluded, and 34 tomograms were selected for PSD density analysis. The gray values within 40 nm range from the postsynaptic membrane were projected to xz plane (Fig. 2) using Fiji[86]. The gray value of each pixel of the projected 2D plane was the average value of the 40 nm column. Next, we used different strategies to process synaptosome and cultured neuron dataset. For synaptosome data, we measured the average gray value in empty space as background gray value. Then we chose the bottom 25% gray values (25% darkest) below the background value for the following clustering analysis. For synapses from cultured neurons, we analyzed the density in the IsoNet[57] corrected tomograms. The data set was normalized after IsoNet internal process, and we chose the bottom 20% gray values (20% darkest) for the following clustering analysis. Lastly, clustering analysis algorithm DBSCAN (density-based spatial clustering of applications with noise) was adopted to do the clustering of PSD density. In the synaptosome sample analysis, DBSCAN with different parameters were performed (Supplementary Fig. 2) and DBSCAN (6, 32) was applied as the results are consistent with the visualized electron density clusters in the tomographic slices. In the synapse analysis, DBSCAN (7, 32) was applied. Positions of tethered, docked, or fused vesicles were projected to the xz plane in the same coordinate system of PSD density to analyze the relation between release sites and PSD clusters. Positions of receptors were also projected to the xz plane in the same coordinate system of PSD density to analyze the relation between receptors and PSD clusters. The area of a nanoblock was defined as its convex hull area shown by red lines in Fig. 2b-c and Supplementary Fig. 2b bottom panel. The width of a nanoblock was defined as the largest x-axis distance between two pixels in the cluster. The widths of nanoblocks are also marked in Figures 2C and the bottom panel of 2D. To precisely measure the height of a

nanoblock, we first averaged the tomographic slices in the range that contains the nanoblock determined in the DBSCAN clustering results. Then we drew a line as shown in Fig. 1c to measure the gray value of the nanoblock in y axis at its largest length. The height of the nanoblock was defined as the distance from the farthest pixel of the nanoblock to the postsynaptic membrane.

Data and code availability

All data reported in this paper will be shared by the lead contact upon request.

References

1 Dieterich, D. C. & Kreutz, M. R. Proteomics of the Synapse--A Quantitative Approach to Neuronal Plasticity. *Molecular & cellular proteomics : MCP* **15**, 368-381 (2016). https://doi.org:10.1074/mcp.R115.051482

2 Perez de Arce, K. *et al.* Topographic Mapping of the Synaptic Cleft into Adhesive Nanodomains. *Neuron* **88**, 1165-1172 (2015). https://doi.org:10.1016/j.neuron.2015.11.011

3 Tang, A. H. *et al.* A trans-synaptic nanocolumn aligns neurotransmitter release to receptors. *Nature* **536**, 210-214 (2016). https://doi.org:10.1038/nature19058

4 MacGillavry, H. D., Song, Y., Raghavachari, S. & Blanpied, T. A. Nanoscale scaffolding domains within the postsynaptic density concentrate synaptic AMPA receptors. *Neuron* **78**, 615-622 (2013). https://doi.org:10.1016/j.neuron.2013.03.009

5 Nair, D. *et al.* Super-resolution imaging reveals that AMPA receptors inside synapses are dynamically organized in nanodomains regulated by PSD95. *The Journal of neuroscience : the official journal of the Society for Neuroscience* **33**, 13204-13224 (2013). https://doi.org:10.1523/JNEUROSCI.2381-12.2013

6 Chamma, I. *et al.* Mapping the dynamics and nanoscale organization of synaptic adhesion proteins using monomeric streptavidin. *Nature communications* **7**, 10773 (2016). https://doi.org:10.1038/ncomms10773

7 Maschi, D. & Klyachko, V. A. Spatiotemporal Regulation of Synaptic Vesicle Fusion Sites in Central Synapses. *Neuron* **94**, 65-73 e63 (2017). https://doi.org:10.1016/j.neuron.2017.03.006

8 Hruska, M., Henderson, N., Le Marchand, S. J., Jafri, H. & Dalva, M. B. Synaptic nanomodules underlie the organization and plasticity of spine synapses. *Nature neuroscience* **21**, 671-682 (2018). https://doi.org:10.1038/s41593-018-0138-9

9 Glebov, O. O. *et al.* Nanoscale Structural Plasticity of the Active Zone Matrix Modulates Presynaptic Function. *Cell Rep* **18**, 2715-2728 (2017).

https://doi.org:10.1016/j.celrep.2017.02.064

10 Martinez-Sanchez, A. *et al.* Trans-synaptic assemblies link synaptic vesicles and neuroreceptors. *Sci Adv* **7** (2021). https://doi.org:10.1126/sciadv.abe6204

11 Frank, R. A. & Grant, S. G. Supramolecular organization of NMDA receptors and the postsynaptic density. *Curr Opin Neurobiol* **45**, 139-147 (2017). https://doi.org:10.1016/j.conb.2017.05.019

12 Kellermayer, B. *et al.* Differential Nanoscale Topography and Functional Role of GluN2-NMDA Receptor Subtypes at Glutamatergic Synapses. *Neuron* **100**, 106-119 e107 (2018). https://doi.org:10.1016/j.neuron.2018.09.012

13 Chen, H., Tang, A. H. & Blanpied, T. A. Subsynaptic spatial organization as a regulator of synaptic strength and plasticity. *Curr Opin Neurobiol* **51**, 147-153 (2018). https://doi.org:10.1016/j.conb.2018.05.004

14 Biederer, T., Kaeser, P. S. & Blanpied, T. A. Transcellular Nanoalignment of Synaptic Function. *Neuron* **96**, 680-696 (2017). https://doi.org:10.1016/j.neuron.2017.10.006

15 Guzikowski, N. J. & Kavalali, E. T. Nano-Organization at the Synapse: Segregation of Distinct Forms of Neurotransmission. *Front Synaptic Neurosci* **13**, 796498 (2021). https://doi.org:10.3389/fnsyn.2021.796498

16 Gramlich, M. W. & Klyachko, V. A. Nanoscale Organization of Vesicle Release at Central Synapses. *Trends Neurosci* **42**, 425-437 (2019). https://doi.org:10.1016/j.tins.2019.03.001

17 Ramsey, A. M. *et al.* Subsynaptic positioning of AMPARs by LRRTM2 controls synaptic strength. *Sci Adv* **7** (2021). https://doi.org:10.1126/sciadv.abf3126

18 Haas, K. T. *et al.* Pre-post synaptic alignment through neuroligin-1 tunes synaptic transmission efficiency. *eLife* **7** (2018). https://doi.org:10.7554/eLife.31755

19 Palay, S. L. Synapses in the central nervous system. *J Biophys Biochem Cytol* **2**, 193-202 (1956). https://doi.org:10.1083/jcb.2.4.193

20 Chen, X. *et al.* Organization of the core structure of the postsynaptic density. *Proceedings of the National Academy of Sciences of the United States of America* **105**, 4453-4458 (2008). https://doi.org:10.1073/pnas.0800897105

21 DeGiorgis, J. A., Galbraith, J. A., Dosemeci, A., Chen, X. & Reese, T. S. Distribution of the scaffolding proteins PSD-95, PSD-93, and SAP97 in isolated PSDs. *Brain Cell Biol* **35**, 239-250 (2006). https://doi.org:10.1007/s11068-007-9017-0

22 Tao, C.-L. *et al.* Differentiation and Characterization of Excitatory and Inhibitory Synapses by Cryo-electron Tomography and Correlative Microscopy. *Journal of Neuroscience* **38**, 1493-1510 (2018). https://doi.org:10.1523/jneurosci.1548-17.2017

23 Chen, X. *et al.* PSD-95 is required to sustain the molecular organization of the postsynaptic density. *The Journal of neuroscience : the official journal of the Society for Neuroscience* **31**, 6329-6338 (2011). https://doi.org:10.1523/JNEUROSCI.5968-10.2011

24 Burette, A. C. *et al.* Electron tomographic analysis of synaptic ultrastructure. *J Comp Neurol* **520**, 2697-2711 (2012). https://doi.org:10.1002/cne.23067

25 Pennacchietti, F. *et al.* Nanoscale Molecular Reorganization of the Inhibitory Postsynaptic Density Is a Determinant of GABAergic Synaptic Potentiation. *The*

Journal of neuroscience : the official journal of the Society for Neuroscience **37**, 1747-1756 (2017). https://doi.org:10.1523/JNEUROSCI.0514-16.2016

26 Crosby, K. C. *et al.* Nanoscale Subsynaptic Domains Underlie the Organization of the Inhibitory Synapse. *Cell Rep* **26**, 3284-3297 e3283 (2019). https://doi.org:10.1016/j.celrep.2019.02.070

27 Zeng, M. *et al.* Reconstituted Postsynaptic Density as a Molecular Platform for Understanding Synapse Formation and Plasticity. *Cell* **174**, 1172-1187 e1116 (2018). https://doi.org:10.1016/j.cell.2018.06.047

28 Zeng, M. *et al.* Phase Transition in Postsynaptic Densities Underlies Formation of Synaptic Complexes and Synaptic Plasticity. *Cell* **166**, 1163-1175 e1112 (2016). https://doi.org:10.1016/j.cell.2016.07.008

29 Feng, Z., Chen, X., Zeng, M. & Zhang, M. Phase separation as a mechanism for assembling dynamic postsynaptic density signalling complexes. *Curr Opin Neurobiol* **57**, 1-8 (2019). https://doi.org:10.1016/j.conb.2018.12.001

30 Taylor, K. A. & Glaeser, R. M. Electron diffraction of frozen, hydrated protein crystals. *Science* **186**, 1036-1037 (1974). https://doi.org:10.1126/science.186.4168.1036

31 Dubochet, J. *et al.* Cryo-electron microscopy of vitrified specimens. *Q Rev Biophys* **21**, 129-228 (1988). https://doi.org:10.1017/s0033583500004297

32 Dubochet, J. & Sartori Blanc, N. The cell in absence of aggregation artifacts. *Micron* **32**, 91-99 (2001). https://doi.org:10.1016/s0968-4328(00)00026-3

33 Bleck, C. K. *et al.* Comparison of different methods for thin section EM analysis of Mycobacterium smegmatis. *Journal of microscopy* **237**, 23-38 (2010). https://doi.org:10.1111/j.1365-2818.2009.03299.x

34 Peet, M. J., Henderson, R. & Russo, C. J. The energy dependence of contrast and damage in electron cryomicroscopy of biological molecules. *Ultramicroscopy* **203**, 125-131 (2019). https://doi.org:10.1016/j.ultramic.2019.02.007

35 Fernandez-Busnadiego, R. *et al.* Quantitative analysis of the native presynaptic cytomatrix by cryoelectron tomography. *The Journal of cell biology* **188**, 145-156 (2010). https://doi.org:10.1083/jcb.200908082

36 Gray, E. G. & Whittaker, V. P. The isolation of nerve endings from brain: an electron-microscopic study of cell fragments derived by homogenization and centrifugation. *J Anat* **96**, 79-88 (1962).

37 Evans, G. J. The synaptosome as a model system for studying synaptic physiology. *Cold Spring Harb Protoc* **2015**, 421-424 (2015). https://doi.org:10.1101/pdb.top074450

38 Hollingsworth, E. B. *et al.* Biochemical characterization of a filtered synaptoneurosome preparation from guinea pig cerebral cortex: cyclic adenosine 3':5'-monophosphate-generating systems, receptors, and enzymes. *The Journal of neuroscience : the official journal of the Society for Neuroscience* **5**, 2240-2253 (1985). https://doi.org:10.1523/JNEUROSCI.05-08-02240.1985

39 Quinlan, E. M., Olstein, D. H. & Bear, M. F. Bidirectional, experience-dependent regulation of N-methyl-D-aspartate receptor subunit composition in the rat visual cortex during postnatal development. *Proceedings of the National Academy of Sciences of the United States of America* **96**, 12876-12880 (1999). https://doi.org:10.1073/pnas.96.22.12876

40 Petersen, J. D. *et al.* Distribution of Postsynaptic Density (PSD)-95 and Ca²⁺/Calmodulin-Dependent Protein Kinase II at the PSD. *The Journal of Neuroscience* **23**, 11270-11278 (2003). https://doi.org:10.1523/jneurosci.23-35-11270.2003

41 Ester, M., Kriegel, H.-P., Sander, J. & Xu, X. in *Proceedings of the Second International Conference on Knowledge Discovery and Data Mining* 226–231 (AAAI Press, Portland, Oregon, 1996).

42 Rahbek-Clemmensen, T. *et al.* Super-resolution microscopy reveals functional organization of dopamine transporters into cholesterol and neuronal activity-dependent nanodomains. *Nat Commun* **8**, 740 (2017). https://doi.org:10.1038/s41467-017-00790-3

43 Natalie, J. G. a. E. T. K. Super-resolution imaging of synaptic scaffold proteins in rat hippocampal neurons. *STAR Protocols* **4**, 102080 (2023). https://doi.org:https://doi.org/10.1016/j.xpro.2023.102080

44 Garcia-Nafria, J., Herguedas, B., Watson, J. F. & Greger, I. H. The dynamic AMPA receptor extracellular region: a platform for synaptic protein interactions. *J Physiol* **594**, 5449-5458 (2016). https://doi.org:10.1113/JP271844

45 Zhao, Y., Chen, S., Swensen, A. C., Qian, W. J. & Gouaux, E. Architecture and subunit arrangement of native AMPA receptors elucidated by cryo-EM. *Science* **364**, 355-362 (2019). https://doi.org:10.1126/science.aaw8250

46 Greger, I. H., Watson, J. F. & Cull-Candy, S. G. Structural and Functional Architecture of AMPA-Type Glutamate Receptors and Their Auxiliary Proteins. *Neuron* **94**, 713-730 (2017). https://doi.org:10.1016/j.neuron.2017.04.009

47 Nakagawa, T., Cheng, Y., Sheng, M. & Walz, T. Three-dimensional structure of an AMPA receptor without associated stargazin/TARP proteins. *Biological chemistry* **387**, 179-187 (2006). https://doi.org:10.1515/BC.2006.024

48 Sobolevsky, A. I., Rosconi, M. P. & Gouaux, E. X-ray structure, symmetry and mechanism of an AMPA-subtype glutamate receptor. *Nature* **462**, 745-756 (2009). https://doi.org:10.1038/nature08624

49 Herguedas, B. *et al.* Structure and organization of heteromeric AMPA-type glutamate receptors. *Science* **352**, aad3873 (2016). https://doi.org:10.1126/science.aad3873

50 Lee, C. H. *et al.* NMDA receptor structures reveal subunit arrangement and pore architecture. *Nature* **511**, 191-197 (2014). https://doi.org:10.1038/nature13548

51 Karakas, E. & Furukawa, H. Crystal structure of a heterotetrameric NMDA receptor ion channel. *Science* **344**, 992-997 (2014). https://doi.org:10.1126/science.1251915

52 El-Husseini, A. E., Schnell, E., Chetkovich, D. M., Nicoll, R. A. & Bredt, D. S. PSD-95 involvement in maturation of excitatory synapses. *Science* **290**, 1364-1368 (2000).

53 Schnell, E. *et al.* Direct interactions between PSD-95 and stargazin control synaptic AMPA receptor number. *Proceedings of the National Academy of Sciences of the United States of America* **99**, 13902-13907 (2002). https://doi.org:10.1073/pnas.172511199

54 Beique, J. C. *et al.* Synapse-specific regulation of AMPA receptor function by PSD-95. *Proceedings of the National Academy of Sciences of the United States of America* **103**, 19535-19540 (2006). https://doi.org:10.1073/pnas.0608492103

55 Elias, G. M. *et al.* Synapse-specific and developmentally regulated targeting of AMPA receptors by a family of MAGUK scaffolding proteins. *Neuron* **52**, 307-320 (2006). https://doi.org:10.1016/j.neuron.2006.09.012

56 Bats, C., Groc, L. & Choquet, D. The interaction between Stargazin and PSD-95 regulates AMPA receptor surface trafficking. *Neuron* **53**, 719-734 (2007). https://doi.org:10.1016/j.neuron.2007.01.030

57 Liu, Y. T. *et al.* Isotropic reconstruction for electron tomography with deep learning. *Nature communications* **13**, 6482 (2022). https://doi.org:10.1038/s41467-022-33957-8

58 Frank, R. A. W., Zhu, F., Komiyama, N. H. & Grant, S. G. N. Hierarchical organization and genetically separable subfamilies of PSD95 postsynaptic supercomplexes. *J Neurochem* **142**, 504-511 (2017). https://doi.org:10.1111/jnc.14056

59 Fernandez, E. *et al.* Targeted tandem affinity purification of PSD-95 recovers core postsynaptic complexes and schizophrenia susceptibility proteins. *Mol Syst Biol* **5**, 269 (2009). https://doi.org:10.1038/msb.2009.27

60 Frank, R. A. *et al.* NMDA receptors are selectively partitioned into complexes and supercomplexes during synapse maturation. *Nature communications* **7**, 11264 (2016). https://doi.org:10.1038/ncomms11264

61 Turk, M. & Baumeister, W. The promise and the challenges of cryo-electron tomography. *FEBS letters* **594**, 3243-3261 (2020). https://doi.org:10.1002/1873-3468.13948

62 Dosemeci, A., Weinberg, R. J., Reese, T. S. & Tao-Cheng, J. H. The Postsynaptic Density: There Is More than Meets the Eye. *Front Synaptic Neurosci* **8**, 23 (2016). https://doi.org:10.3389/fnsyn.2016.00023

63 Vyas, Y. & Montgomery, J. M. The role of postsynaptic density proteins in neural degeneration and regeneration. *Neural Regen Res* **11**, 906-907 (2016). https://doi.org:10.4103/1673-5374.184481

64 Broadhead, M. J. *et al.* PSD95 nanoclusters are postsynaptic building blocks in hippocampus circuits. *Scientific reports* **6**, 24626 (2016). https://doi.org:10.1038/srep24626

65 Sheng, M. & Hoogenraad, C. C. The postsynaptic architecture of excitatory synapses: a more quantitative view. *Annual review of biochemistry* **76**, 823-847 (2007). https://doi.org:10.1146/annurev.biochem.76.060805.160029

66 Kaizuka, T. & Takumi, T. Postsynaptic density proteins and their involvement in neurodevelopmental disorders. *J Biochem* **163**, 447-455 (2018). https://doi.org:10.1093/jb/mvy022

67 Zeng, M., Ye, F., Xu, J. & Zhang, M. PDZ Ligand Binding-Induced Conformational Coupling of the PDZ-SH3-GK Tandems in PSD-95 Family MAGUKs. *Journal of molecular biology* **430**, 69-86 (2018). https://doi.org:10.1016/j.jmb.2017.11.003

68 Hassani Nia, F. *et al.* Structural deficits in key domains of Shank2 lead to alterations in postsynaptic nanoclusters and to a neurodevelopmental disorder in humans. *Molecular psychiatry* (2022). https://doi.org:10.1038/s41380-022-01882-3

69 Chen, X. *et al.* PSD-95 family MAGUKs are essential for anchoring AMPA and NMDA receptor complexes at the postsynaptic density. *Proceedings of the National Academy of Sciences of the United States of America* **112**, E6983-6992 (2015).

https://doi.org:10.1073/pnas.1517045112

70 Dutta, A. *et al.* Cooperative Dynamics of Intact AMPA and NMDA Glutamate Receptors: Similarities and Subfamily-Specific Differences. *Structure* **23**, 1692-1704 (2015). https://doi.org:10.1016/j.str.2015.07.002

71 Krieger, J., Bahar, I. & Greger, I. H. Structure, Dynamics, and Allosteric Potential of Ionotropic Glutamate Receptor N-Terminal Domains. *Biophysical journal* **109**, 1136-1148 (2015). https://doi.org:10.1016/j.bpj.2015.06.061

72 Durr, K. L. *et al.* Structure and dynamics of AMPA receptor GluA2 in resting, pre-open, and desensitized states. *Cell* **158**, 778-792 (2014). https://doi.org:10.1016/j.cell.2014.07.023

73 Meyerson, J. R. *et al.* Structural mechanism of glutamate receptor activation and desensitization. *Nature* **514**, 328-334 (2014). https://doi.org:10.1038/nature13603

74 Geinisman, Y. *et al.* Structural synaptic correlate of long-term potentiation: formation of axospinous synapses with multiple, completely partitioned transmission zones. *Hippocampus* **3**, 435-445 (1993). https://doi.org:10.1002/hipo.450030405

75 Stewart, M. G. *et al.* Chemically induced long-term potentiation increases the number of perforated and complex postsynaptic densities but does not alter dendritic spine volume in CA1 of adult mouse hippocampal slices. *Eur J Neurosci* **21**, 3368-3378 (2005). https://doi.org:10.1111/j.1460-9568.2005.04174.x

76 Nieto-Sampedro, M., Hoff, S. F. & Cotman, C. W. Perforated postsynaptic densities: probable intermediates in synapse turnover. *Proceedings of the National Academy of Sciences of the United States of America* **79**, 5718-5722 (1982). https://doi.org:10.1073/pnas.79.18.5718

77 Sturgill, J. F., Steiner, P., Czervionke, B. L. & Sabatini, B. L. Distinct Domains within PSD-95 Mediate Synaptic Incorporation, Stabilization, and Activity-Dependent Trafficking. *The Journal of Neuroscience* **29**, 12845-12854 (2009). https://doi.org:10.1523/jneurosci.1841-09.2009

78 Alten, B. *et al.* Role of Aberrant Spontaneous Neurotransmission in SNAP25-Associated Encephalopathies. *Neuron* **109**, 59-72 e55 (2021). https://doi.org:10.1016/j.neuron.2020.10.012

79 Sun, R. *et al.* An efficient protocol of cryo-correlative light and electron microscopy for the study of neuronal synapses. *Biophysics Reports* **5**, 111-122 (2019). https://doi.org:10.1007/s41048-019-0092-4

80 Hagen, W. J. H., Wan, W. & Briggs, J. A. G. Implementation of a cryo-electron tomography tilt-scheme optimized for high resolution subtomogram averaging. *Journal of structural biology* **197**, 191-198 (2017). https://doi.org:10.1016/j.jsb.2016.06.007

81 williamnwan/TOMOMAN: TOMOMAN 08042020 v. 08042020 (Zenodo, 2020).

82 Zheng, S. Q. *et al.* MotionCor2: anisotropic correction of beam-induced motion for improved cryo-electron microscopy. *Nat Methods* **14**, 331-332 (2017). https://doi.org:10.1038/nmeth.4193

83 Zhang, K. Gctf: Real-time CTF determination and correction. *Journal of structural biology* **193**, 1-12 (2016). https://doi.org:10.1016/j.jsb.2015.11.003

84 Kremer, J. R., Mastronarde, D. N. & McIntosh, J. R. Computer visualization of three-dimensional image data using IMOD. *Journal of structural biology* **116**, 71-

76 (1996). https://doi.org:10.1006/jsbi.1996.0013

85 Bharat, T. A. & Scheres, S. H. Resolving macromolecular structures from electron cryo-tomography data using subtomogram averaging in RELION. *Nat Protoc* **11**, 2054-2065 (2016). https://doi.org:10.1038/nprot.2016.124

86 Schindelin, J. *et al.* Fiji: an open-source platform for biological-image analysis. *Nat Methods* **9**, 676-682 (2012). https://doi.org:10.1038/nmeth.2019

Fig. 1

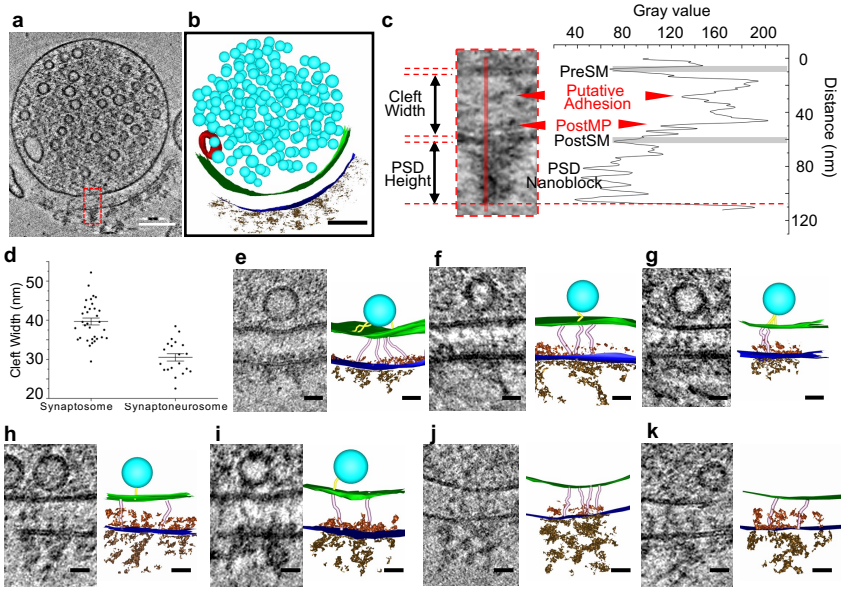
a
b
c
Gray value
40
80
120
160
200
Cleft Width
PSD Height
PreSM
Putative Adhesion
PostMP
PostSM
PSD Nanoblock
0
40
80
120
Distance (nm)
d
Cleft Width (nm)
50
40
30
20
Synaptosome
Synaptoneurosome
e
f
g
h
i
j
k

Fig. 2

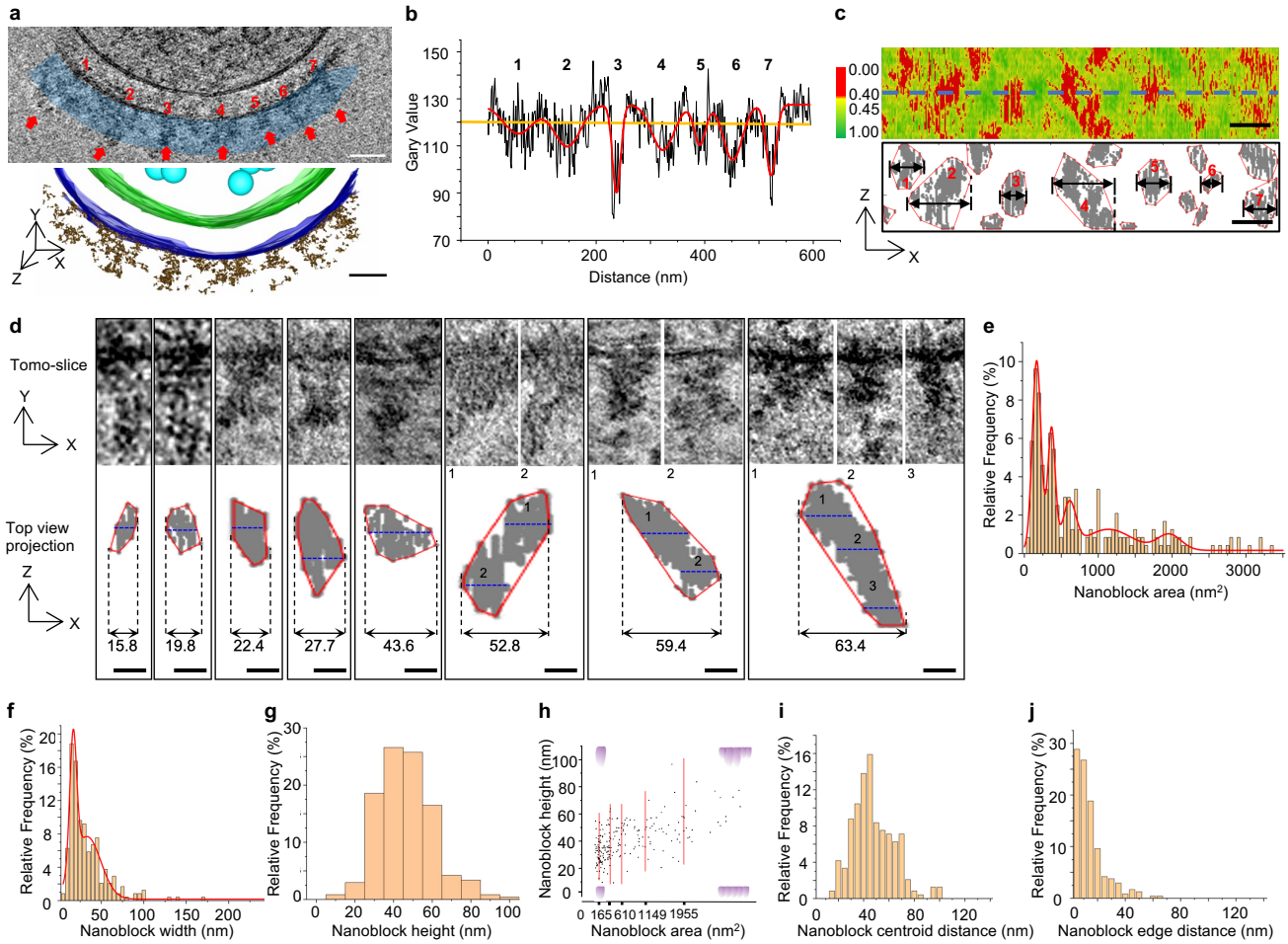
a
b
c
Gary Value
Distance (nm)
0.00
0.40
0.45
1.00
d
Tomo-slice
Top view projection
15.8
19.8
22.4
27.7
43.6
52.8
59.4
63.4
e
Relative Frequency (%)
Nanoblock area (nm²)
f
Nanoblock width (nm)
g
Nanoblock height (nm)
h
Nanoblock height (nm)
Nanoblock area (nm²)
i
Nanoblock centroid distance (nm)
j
Nanoblock edge distance (nm)

Fig. 3

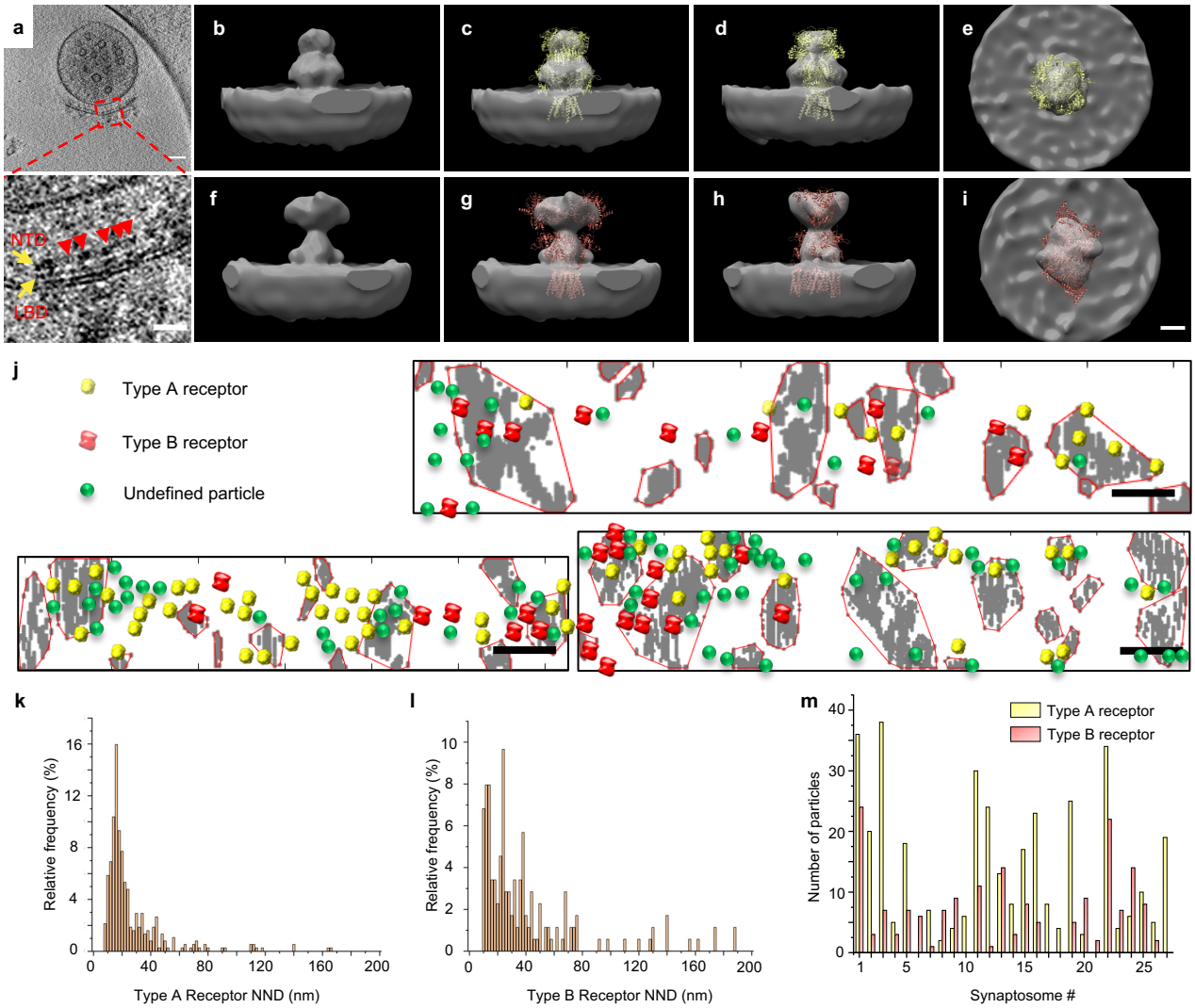
a
b
c
d
e
f
g
h
i
NTD
LBD
j
Type A receptor
Type B receptor
Undefined particle
k
Relative frequency (%)
Type A Receptor NND (nm)
l
Relative frequency (%)
Type B Receptor NND (nm)
m
Type A receptor
Type B receptor
Number of particles
Synaptosome #

Fig. 4

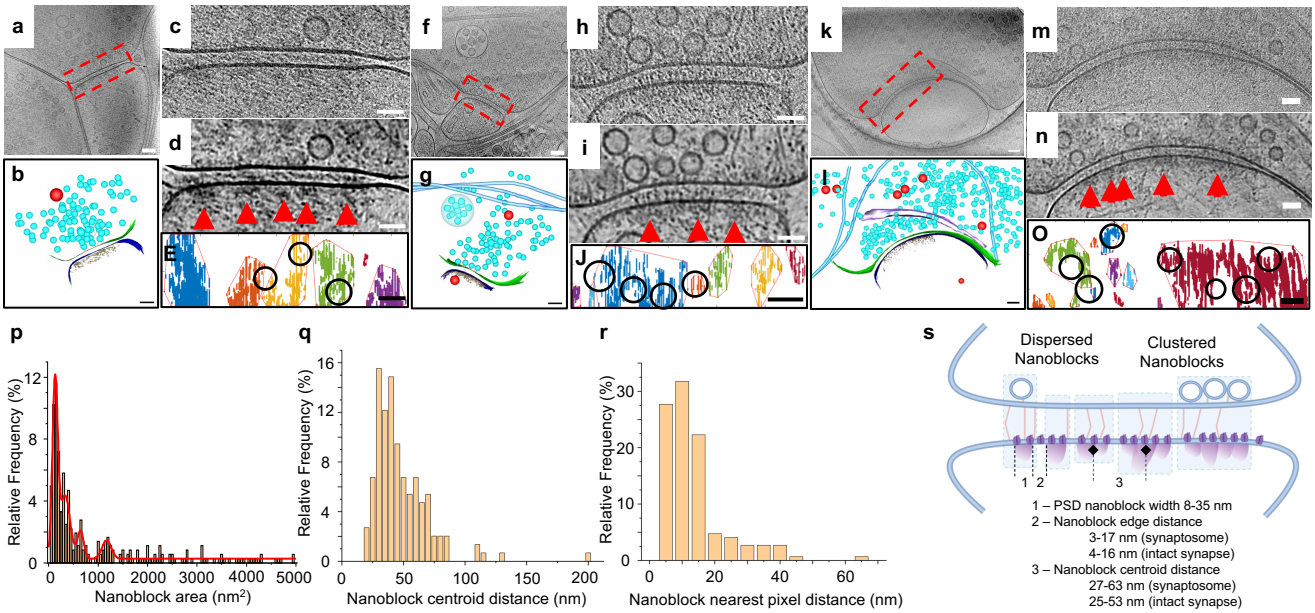
a
b
c
d
E
f
g
h
i
J
k
l
m
n
O
p
Relative Frequency (%)
Nanoblock area (nm²)
q
Relative Frequency (%)
Nanoblock centroid distance (nm)
r
Relative Frequency (%)
Nanoblock nearest pixel distance (nm)
s
Dispersed Nanoblocks
Clustered Nanoblocks
1 – PSD nanoblock width 8-35 nm
2 – Nanoblock edge distance
3-17 nm (synaptosome)
4-16 nm (intact synapse)
3 – Nanoblock centroid distance
27-63 nm (synaptosome)
25-53 nm (intact synapse)

Supplementary Fig. 1

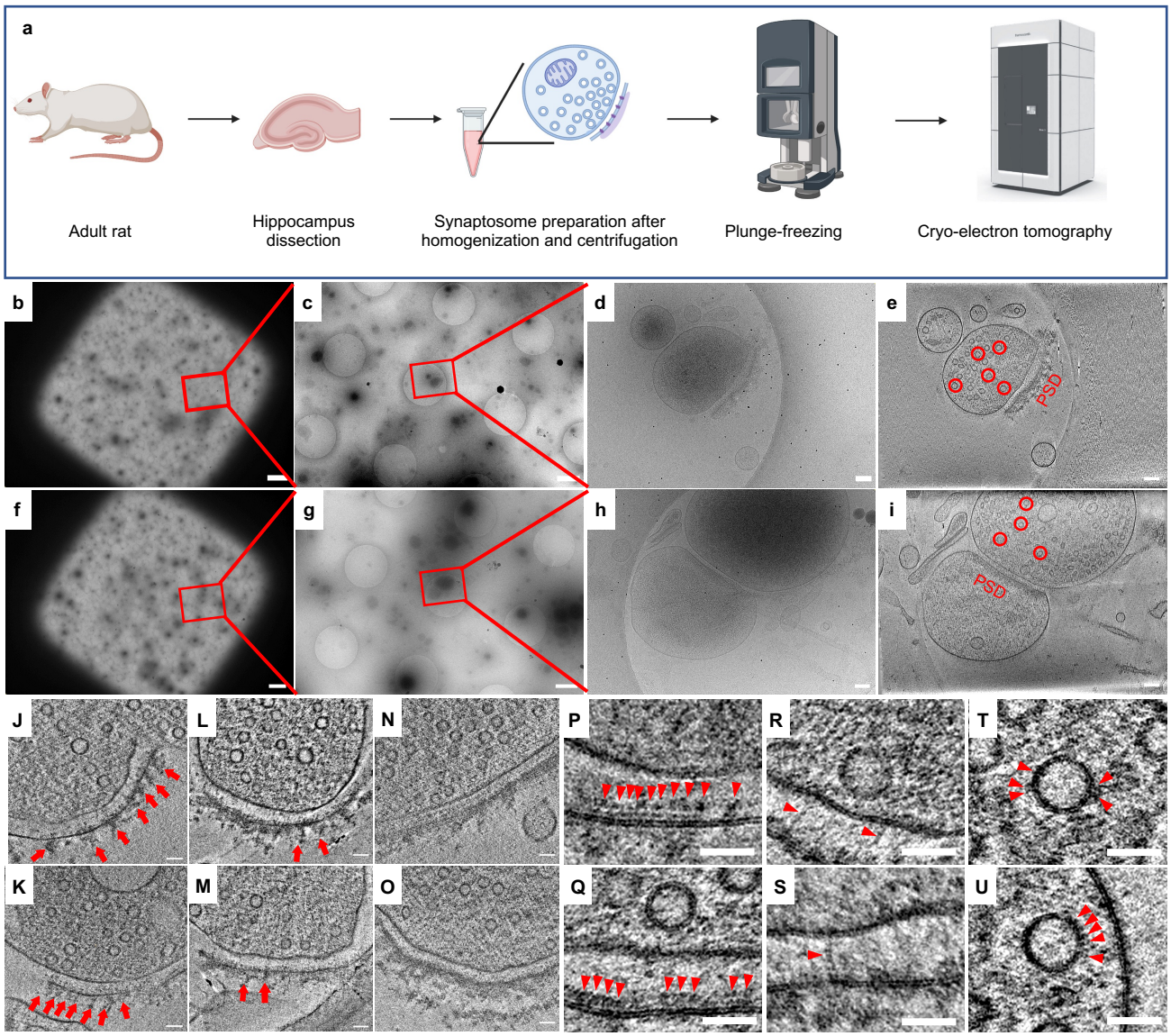

Supplementary Fig. 2

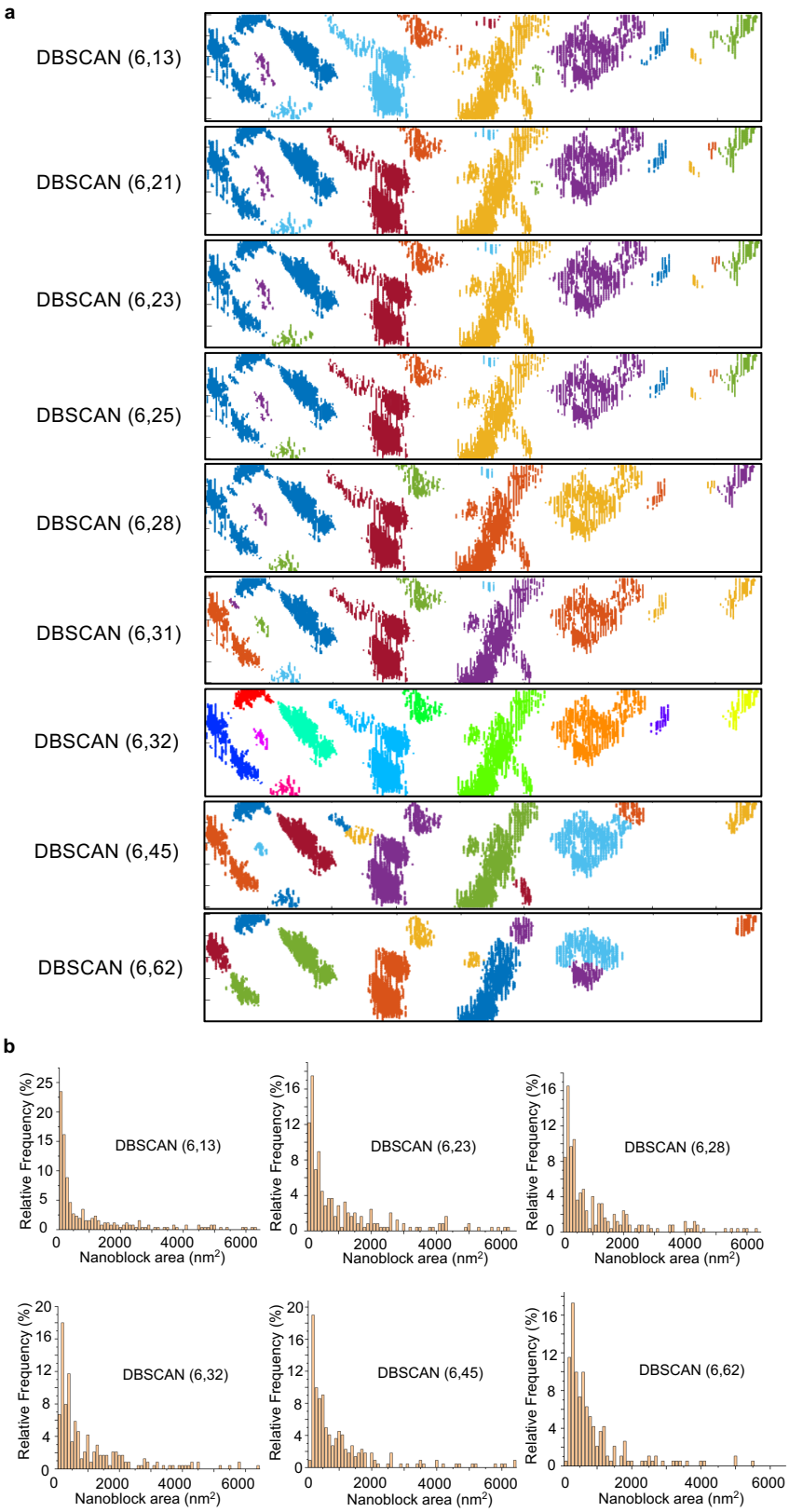

Supplementary Fig. 3

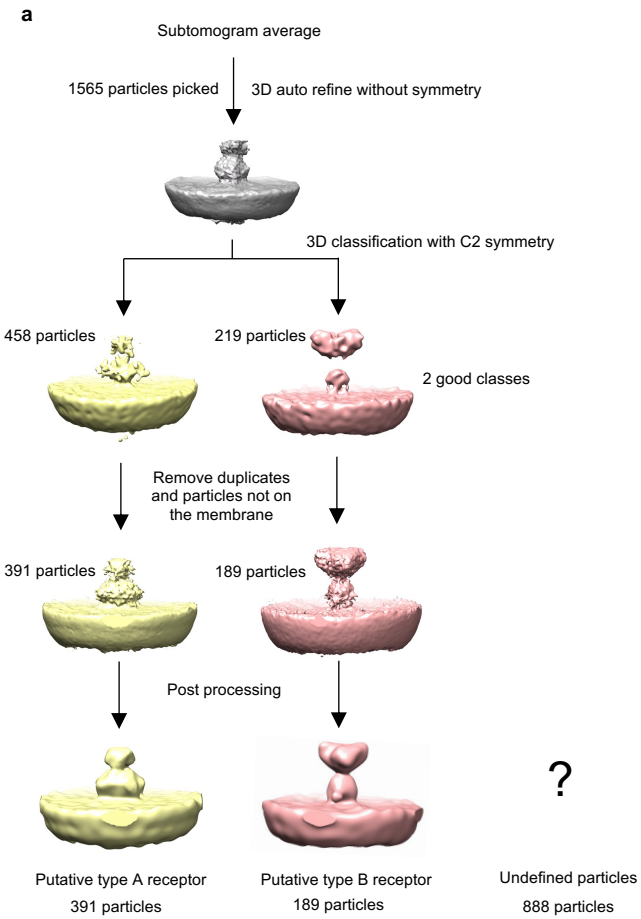

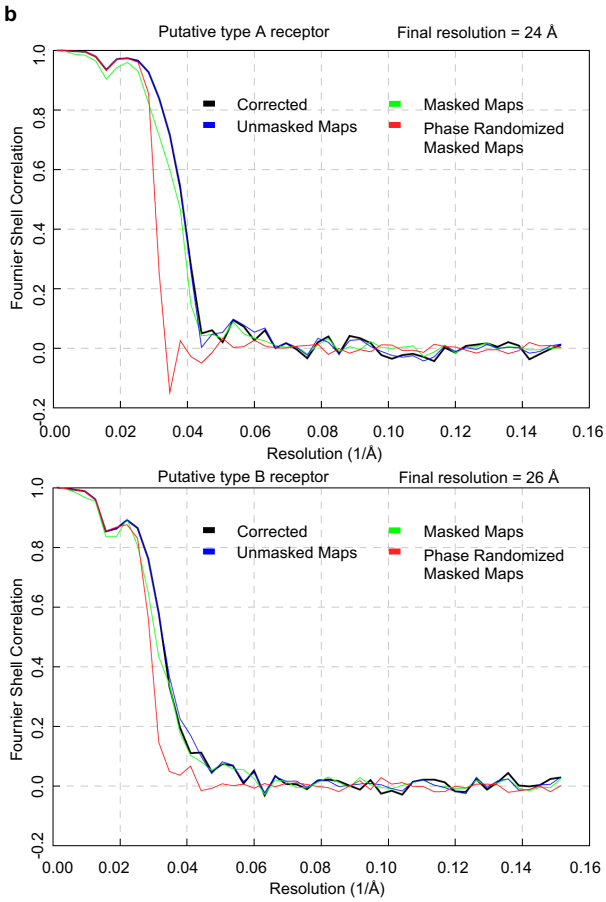
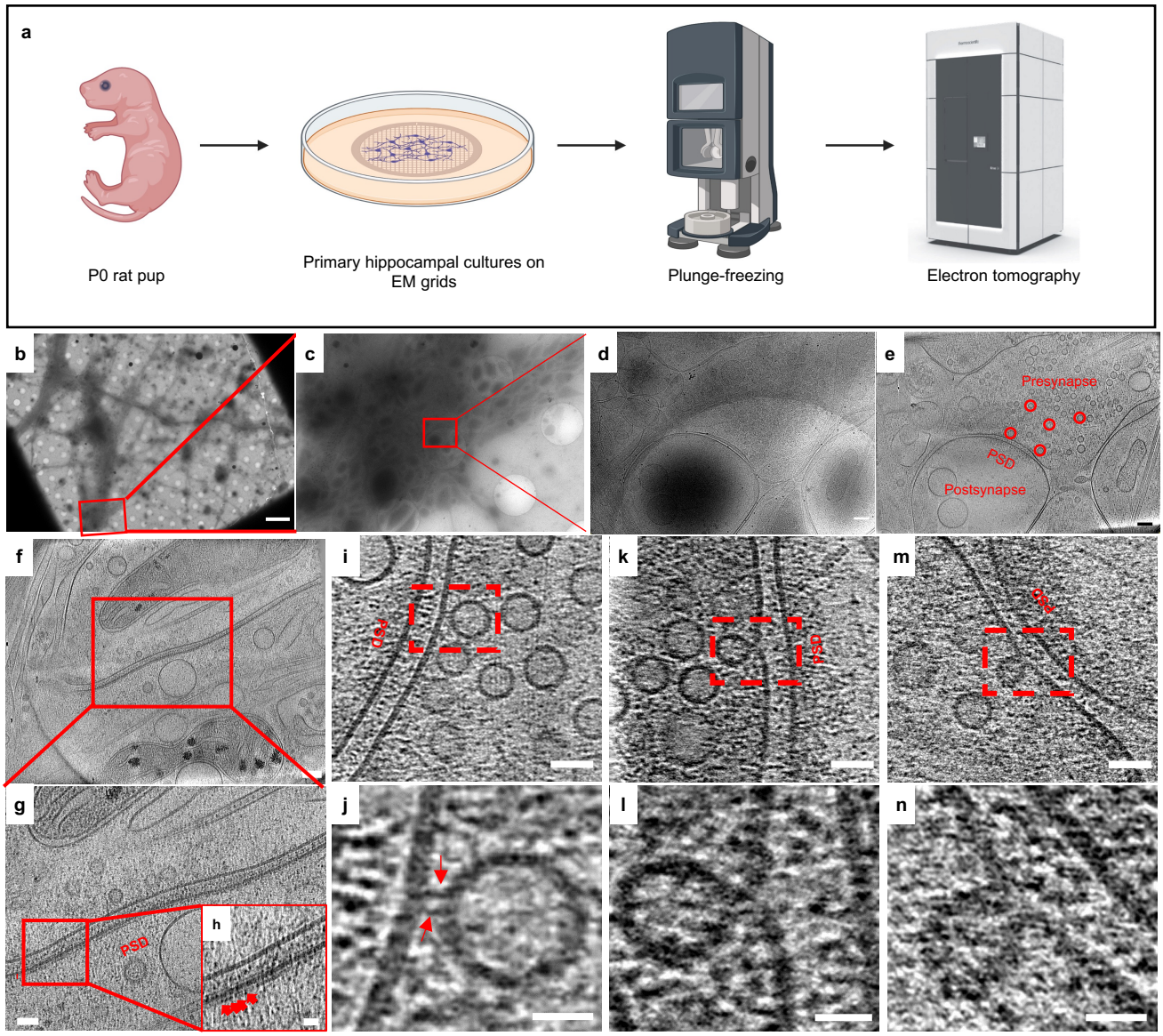
Supplementary Fig. 4